Additively manufactured steel reinforcement for small scale reinforced concrete modeling: Tensile and bond behavior

Materials & Design 241 (2024) 112919

Contents lists available at ScienceDirect

Materials & Design

journal homepage: www.elsevier.com/locate/matdes

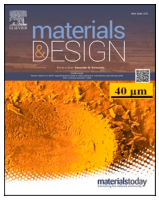

Additively manufactured steel reinforcement for small scale reinforced concrete modeling: Tensile and bond behavior

Medhat Elmorsy [a,b], Rafal Wrobel [c], Christian Leinenbach [c,d], Michalis F. Vassiliou [a,*]

[a] Chair of Seismic Design and Analysis, Institute of Structural Engineering, ETH Zürich, Zürich, Switzerland
[b] Structural Engineering Dept. Mansoura University, Mansoura, Egypt
[c] Empa, Swiss Federal Laboratories for Materials Science and Technology, Dübendorf, Switzerland
[d] Laboratory for Photonic Materials and Characterization, École Polytechnique Fédérale de Lausanne (EPFL), Lausanne, Switzerland

ARTICLE INFO

Keywords:
Additive manufacturing
Centrifuge testing
Physical modelling
Small-scale models
RC structures
Bond
Earthquake engineering

ABSTRACT

Small scale (~1:30–1:40) Reinforced Concrete is useful for centrifuge testing. However, manufacturing the reinforcing cages by hand at this scale is practically difficult. This paper suggests that small scale reinforcement can be manufactured using a metal 3D printer. Mechanical properties of 3D printed submillimeter rebars are discussed and compared to properties of typical prototype rebars. Different model concrete mix designs are tested to identify optimal mixes. Pullout tests of rebars with different surface rib configurations embedded in different concrete mixes are discussed.

Based on the test results, by modulating the printing parameters it seems feasible to obtain 3D printed submillimeter bars that can be used as physical models of prototype rebars. A gypsum-based model concrete was more similar to prototype concrete than cement-based mixes. Most importantly, bond slip behavior that is comparable to full-scale concrete could be achieved, something that is vital and has never been reported before.

1. Introduction

Experimental testing is a cornerstone of the Scientific Method. Moncarz and Krawinkler [1] identified three basic objectives for which experimental testing is generally conducted; (a) develop or verify component-level force deformation relationships, (b) establish loading criteria for environmental loads such as wind and earthquakes, and (c) study of the structure-level behavior. The purpose of studying the structure-level behavior can be validation of analytical methods/studies or demonstration of the structural safety/integrity of structural systems.

Within the context of Earthquake Engineering, results of blind prediction contests of shake table tests document the inability of state-of-the-art models to predict the dynamic response of Reinforced Concrete (RC) structures with a reasonable accuracy, therefore question the validity of seismic design processes [2]. In these contests, expert teams are invited to numerically predict the results of a shake table experiment on a part of or on a whole structure. The predictions have high scatter and, in some cases, are wrong by multiple folds. For instance, the blind prediction contest organized on the shake table tests of a slice of a shear wall building tested in [3] showed that there was a high scatter between model predictions and overall poor performance of the competing models. The poor performance of the numerical models happened despite the fact that in such contests, the material level uncertainty is reduced by providing to the contestants the experimentally obtained material properties. Moreover, blind prediction contests for component-level tests show much better results than the system-level ones [4,5]. These observations emphasize the importance of validation of the global level assumptions (e.g. formulation of global damping, boundary conditions, component interaction). In fact, Bradley [6] claimed that it is not the material or component level assumptions, but the transition from component- to system- level that induces the largest error (Fig. 1). Quantifying system-level assumptions requires sub-system or system-level experimental testing, which is costly and very time-consuming at large scales [7].

In parallel, it has recently been argued that model validation in Earthquake Engineering should involve testing under a large bin of excitations [8–11]. In fact, Bachmann et al. [8] studied the response of a rocking block under single and multiple (i.e. a bin of 100) excitations. They concluded that a widely used analytical model was not able to predict the response to single ground motions, but it managed to predict the Cumulative Distribution Function (CDF) of the temporal maxima of the responses to a bin of ground motions, because even though the

* Corresponding author at: Stefano-Franscini-Platz 5, CH-8093 Zürich, Switzerland.
E-mail address: vassiliou@ibk.baug.ethz.ch (M.F. Vassiliou).

https://doi.org/10.1016/j.matdes.2024.112919
Received 5 June 2023; Received in revised form 2 April 2024; Accepted 6 April 2024
Available online 10 April 2024

model was not accurate, it was unbiased. As seismic design involves predicting the statistics of the response to a set of ground motions rather than to a single one, Bachmann et al. [8] argued that predicting the CDF is a sufficient test for a numerical model to be useful and named the procedure "statistical (or weak) validation procedure".

If one tries to apply the statistical validation procedure to validate global level assumptions of RC numerical models there is an obvious difficulty: One would need a virgin specimen for each ground motion of the bin. Given the cost of full-scale shake table testing, this is impossible at full scale. It is even not cost-wise efficient at the usual scales that shake table tests of RC structures are performed (no less than 1:3–1:5). This is why this paper identifies the usefulness (and, maybe, the need) for small scale testing (say 1:30 to 1:40) focusing exclusively on what cannot be validated at component level: The global level assumptions. At a such a small scale (on the order of 1:30 – 1:40) such tests need to be performed in a geotechnical centrifuge to preserve similitude of stresses.

The authors acknowledge the counterargument: Moncarz and Krawinkler [1] indicated that for a model to be trusted it should preferably be no smaller than 1/3 scale, as smaller physical models induce unacceptable physical distortion. Bazant and Planas have also documented the scale dependence of concrete properties [12], which is also discussed in the classic textbook of Harris and Sabnis [13]. However, according to Del Giudice et al. [14] "it is acknowledged that a 1:30–1:40 model will be unavoidably distorted, as concrete properties scale with size, even when scaled aggregates are used. However, the purpose of this approach (i.e. of small-scale shake table tests focusing exclusively on global level assumptions) is not to create undistorted models but to statistically validate the global level assumptions (Fig. 1) for given and experimentally obtained (at the model scale) component level behavior. Therefore, it needs to be clarified that the purpose of small-scale tests is not to determine the component level behavior of full-scale RC members. This can and should be determined by tests as close as possible to full scale." Moreover, Del Giudice et al. [14] claim that such a methodology "is easier to apply to modern structures that are designed to be ductile and fail by forming plastic hinges – a failure mechanism that is less influenced by scale phenomena.".

At such a small scale, it is practically difficult to manufacture small scale RC specimens by hand, as the reinforcing cages become extremely small to be handled manually [15,16]. Additive manufacturing (AM) can provide a solution to this problem. In addition, AM can be used to manufacture the tiny concrete formworks. Feasibility studies [14] of this approach have already been performed. Based on these studies which included material and component level testing, manufacturing of 1:40 scale models is construction-wise possible and their structural behavior was generally similar to that predicted by numerical models. However, the tests conducted in [14] presented two major issues: The model concrete had too high tensile strength and the developed bond strength between the printed rebars and the concrete was too high. As a result, there was much smaller strain penetration than that in prototype scale and the rebars of a model RC beam fractured prematurely under cyclic loading.

Therefore, preserving similitude (as much as possible) of tensile behavior of concrete and of the bond strength between the rebars and the concrete when scaling down the models is vital since it affects the failure mode, the ductility and the cracking load levels and patterns [13]. The bond strength depends on adhesion and friction over the surface of the rebar at low bond stresses. Near and post ultimate bond strength, bond relies increasingly on the bearing of the ribs on the concrete [17]. Hence, by modulating the concrete mix design and bar surface rib configuration, one can attempt to persevere bond similitude between concrete and reinforcement.

This paper presents and discusses the mechanical properties of additively manufactured submillimeter steel reinforcing bars for use in small scale modeling of RC structures in a geotechnical centrifuge. These mechanical properties are obtained through series of tests performed on plain and deformed bars using different manufacturing (printing) parameters. Subsequently, this paper discusses pullout tests that are performed to characterize the similitude of the local bond slip behavior between the 3D printed rebars and full-scale bond slip behavior.

2. Steel Additive manufacturing

Additive manufacturing (AM) digital techniques for metals – often termed '3D-printing' – are powder based, layer by layer methods which can directly build metallic 3D structures with intricate geometries and new functionalities [18]. Two main additive manufacturing techniques for metals are identified: powder bed based (Laser Powder Bed Fusion, short: L-PBF) and flow based (Direct Metal Deposition, short: DMD). In both processes, a metallic powder is consolidated in a layer-by-layer manner by rapid melting and solidification. In the L-PBF process, metal powder is melted by the energy of a laser beam. After the laser has melted one layer, a new layer of powder is added to the resulting work piece. Then, the laser is used again to melt the next layer and this procedure is repeated until a desired geometry is achieved. On the other hand, the powder is blown into a melt pool in the DMD process. L-PBF and DMD have several advantages over conventional manufacturing processes. They create fully dense and complex parts with almost any geometry. In comparison with L-PBF, DMD is characterized by a larger laser spot diameter (1–4 mm for DMD vs. 50–100 μm for L-PBF), lower laser scan velocities, and thicker layer thickness. The resulting feature sizes are therefore on the order of several millimeters for DMD, while features as small as 250–300 μm can be fabricated with L-PBF [18,19]. Considering all the above listed advantages and disadvantages of both technologies, L-PBF was selected to be used in the scope of presented work. Fig. 2a shows the L-PBF technology principal process.

Low-alloyed steels or carbon steels, which are typically used in civil engineering applications, have been only scarcely studied (in the context of metal AM) as they undergo a martensitic transformation during the very rapid consolidation, resulting in a very brittle microstructure and cracking. Therefore, in this study, an austenitic 316L stainless steel was used. It is characterized by good laser processability in comparison to other steels that are more susceptible to cracks formation. Moreover, it

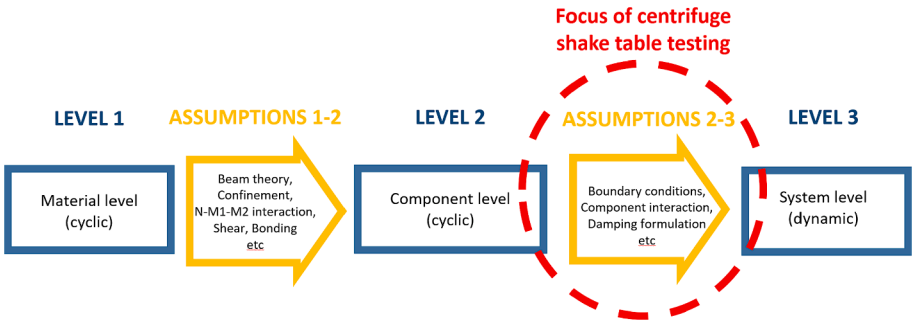

Fig. 1. Schematic representation of material to component to system level transition.

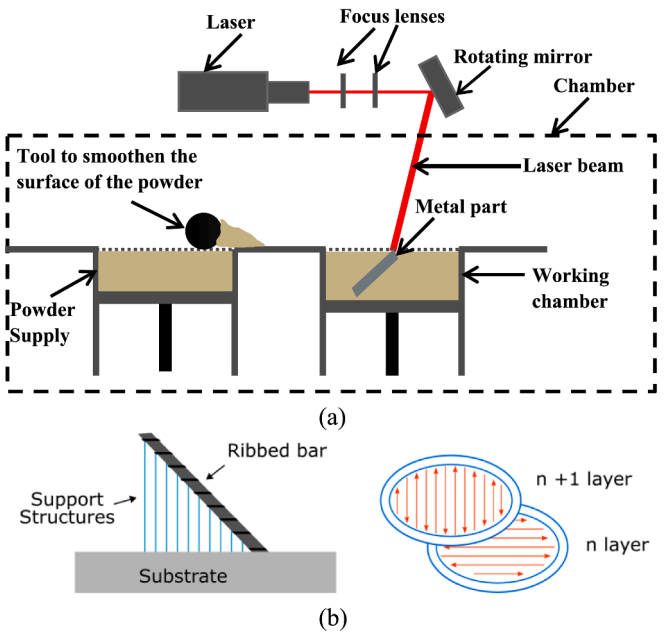

Fig. 2. (a) Laser powder bed fusion (L-PBF) feed and manufacturing system (b) scanning strategy.

has good corrosion resistance compared to other steels from the same group (e.g. 304 steel). The mechanical properties of L-PBF 316L stainless steel can be varied in a relatively wide range by carefully adjusting the AM processing parameters and/or applying subsequent heat treatments [20]. However, even though we can control the microstructure and mechanical properties by adjusting different process parameters, the mechanical properties will differ in comparison to, for instance, wrought steel. The main reason is the thermal history that leads to high cooling rates, resulting in a very fine microstructure.

In this study, a gas-atomized 316L stainless steel powder with a particle size distribution of 45 ± 15 μm (provider: Oerlikon AM) was used to fabricate the steel reinforcement bars. The steel reinforcement bars were fabricated using a Concept Laser M2 L-PBF machine equipped with a 200 W 1070 nm fiber laser operating in continuous mode with a Gaussian intensity distribution and 90 μm spot size. The build volume comprises 245 x 245 mm build plate and 285 mm maximum build height.

3. Test program and specimens

3.1. Tensile test of reinforcing bars

Bars were manufactured using previously optimized processing parameters on (simple) cubic samples with dimensions 10x10x10 mm^3. These processing parameters were 110 W of laser power, a scanning speed of 300 mm/s, a layer thickness of 0.03 mm, and hatch spacing of 0.01 mm. The printing parameters were selected to produce favorable mechanical properties (for the specific application of RC structures modeling) comparable to full scale construction. All bars were fabricated inclined at 45° with the respect to the base plate in order to fit as big as possible samples. Therefore, despite the overall minor anisotropy of the printed material, inherent in the printing process, this is not expected to influence the uniaxial properties of the rebars. Moreover, a support structure (made of steel) was used to dissipate the heat produced during laser processing into the build plate and to avoid any distortion of the parts during fabrication. It was relatively easy to manually remove it (with a tweezer) because the support was designed to be weak (i.e. of reduced cross section), especially at the connection point with the part. For bars fabrication, a unidirectional scanning strategy with 90° rotation between layers has been applied (Fig. 2b– red arrows) with additional contour scans (Fig. 2b – blue arrows) to ensure a high quality of the fabricated parts. The distance between the contour and the fill (contour spacing) was 0.075 mm. However, after fabricating a first batch of the samples (denoted batch I), it turned out that a problem occurred when transferring the parameters optimized from cubic samples to the thin-strutted reinforcing bars. The fabricated bars showed pronounced residual porosity in the close vicinity of the bar edges indicating insufficient contour and fill overlap, which affected the mechanical properties, as discussed later in this paper.

Consequently, small adjustments were made to the contour spacing. Hence, a second batch (denoted batch II) of rebars was printed with a double contour and a contour spacing of 0.06 mm, achieving a significantly higher density of fabricated specimens. The metallographic cross-sections in Fig. 3 show a comparison of two bars from the first and the second batch of rebars. A post-process heat treatment at 600 °C for 6 hours followed by slow cooling to room temperature was applied to one of the optimized batches (denoted batch III) to relieve residual stresses and study its effect on the mechanical behavior. A summary of the various processing parameters for the three batches used in the study is shown in Table 1. Two rebar diameters were tested; 0.8 mm and 0.4 mm, corresponding to 24 mm and 12 mm reinforcing bars at 1:30 scaled models. Six rebar samples were tested for each diameter to evaluate the scatter of tensile test results among similar rebars.

In order to study the mechanical properties of the 3D printed reinforcing bars, three batches of steel reinforcing bars. In addition, different rebar surface rib configurations were tested. This is due to the fact that the bond between concrete and reinforcing steel bars should be similar to the bond in prototype Reinforced Concrete in order to physically model the interaction between the two constituents of the RC material and replicate the failure and cracking modes. For the tensile test, two configurations were tested; plain rebars (P) and ribbed rebars with rib configuration D1 that had the rib parameters shown in Table 2. Notably, as there is an inherent roughness of the rebars (R_a on the order of 30 μm), plain rebars are not as smooth as their full-scale counterparts [14]. Fig. 4 (left) shows the definition of the rib parameters in Table 2 (rib height (h), rib spacing (c), and rib inclination angle (β)) according to the definition of EN:10080 standard [21]. The rebar with 0.4 mm diameter was only tested with plain surface (without ribs) for two reasons: 1. when printing the rebar with ribs, the ribs were barely printed due to the insufficient accuracy of the printer for such small details and 2. the 0.4 mm rebar was intended to be used as shear reinforcement (stirrups) in the proposed framework which could not have ribs. Three variations of rib configurations (D1, D2, and D3) were chosen to cover the range suggested by EN:10080 standard with D2 being the least dense and D3 the densest configuration. Plain rebars were tested to check the sufficiency of inherent roughness to generate enough bond with concrete as discussed in a subsequent section. Fig. 4 (right) shows the build plate with the rebars printed with 45° angle. Images taken with an optical microscope were used to measure the actual diameter of the rebars and to check the general surface roughness of the rebars. Fig. 5 shows examples of such optical microscopy.

3.2. Concrete compression and four-point bending tests

Seven concrete mixes were used to perform mechanical tests in order to identify mixes with mechanical properties that are comparable to prototype scale concrete. Four types of binder were tried according to Table 3. For the mix with cement binder (mix A), one water binder ratio (W/B = 0.5) was tested. For the mixes with gypsum as binder, two water binder ratios were used; 1.0 according to tests performed by Knappett et al. [16] and 0.5:0.7 (depending on the type of the binder) as recommended by the binder manufacturer. For all the mixes, the sand binder ratio (S/B) was kept constant at 1.0 based on previous studies by [14,16]. The sand used in all mixes was Perth silica sand (Crystaline silica SiO_2) with a d_{50} = 0.23 mm – Its grain distribution compares well

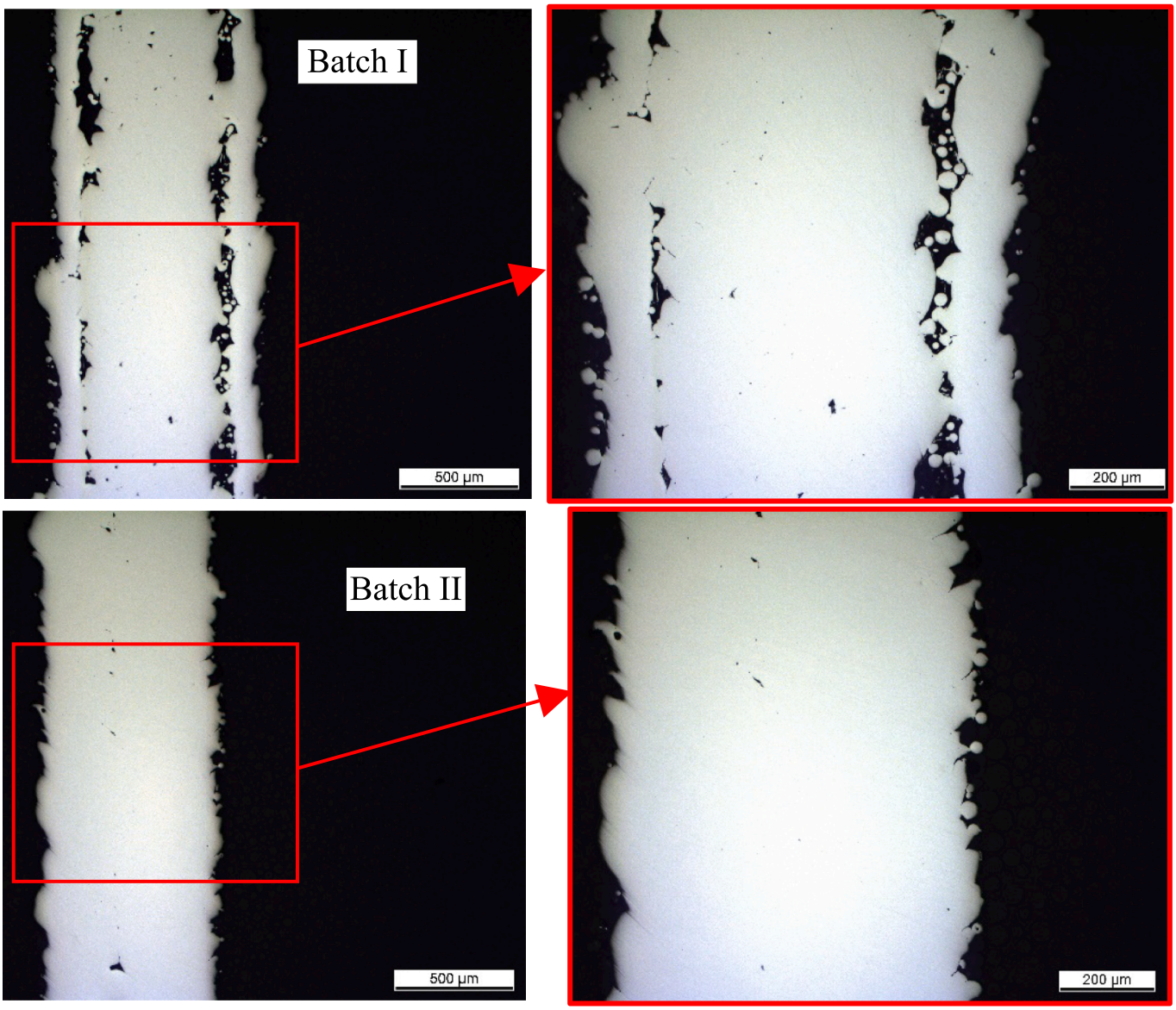

Fig. 3. Cross sections of the rebars from batches I and II showing the better density (less porosity) in batch II.

Table 1
Printing characteristics of the tensile test specimen batches.

Batch	Laser power [W]	Scanning speed [mm/s]	Hatch spacing [mm]	Layer thickness [mm]	Printing orientation [°]	Number of contours	Contour distance [mm]	Heat Treatment
I	110	300	0.01	0.03	45	1	0.075	No
II	110	300	0.01	0.03	45	2	0.06	No
III	110	300	0.01	0.03	45	2	0.06	Yes

Table 2
Ribs parameters for the three tested rib configurations.

Category	*h*	*c*	*β*
EN:10080 [21] recommended range	0.03d:0.15d*	0.40d:1.20d	35°:75°
D1	0.10d	1.00d	63.43°
D2	0.05d	1.20d	63.43°
D3	0.15d	0.50d	63.43°

*d is the rebar diameter.

to the typical aggregate size when scaled 30–40 times as shown by [14]. The testing of the cement concrete mix was tested first based on a previous study by Del Giudice et al. [14] that showed that the cement concrete compressive strength, tensile strength, and bond behavior was not similar to that of the prototype ones as discussed later in this paper. Therefore, the other mixes (mix B: mix G) were attempted.

Cylinders of diameter 15 mm and height 30 mm were tested under uniaxial compression. For the four-point bending test, beams with 15 mm x 15 mm cross section and 80 mm length (shear span was equal to 20 mm). For each mix, six cylinders and six beams were tested to evaluate the dispersion of flexural and compression strength. A PLA (Polylactic acid) 3D printer was used to print the beam molds while for

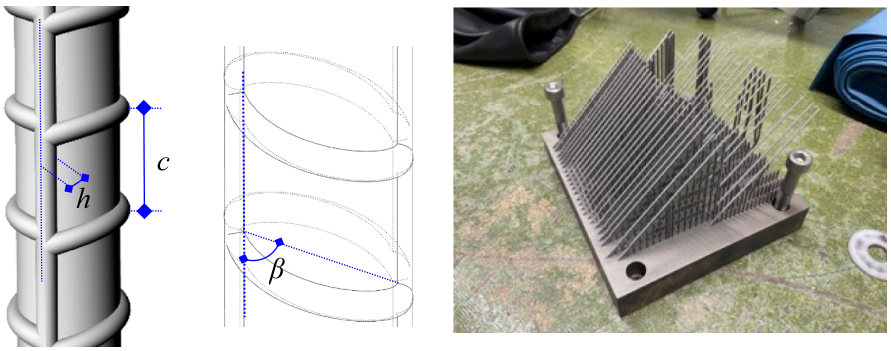

Fig. 4. Left: Rebar surface ribs details according to EN:10080 standard [21], Right: The base plate showing the 3D printed rebars attached to the base plate.

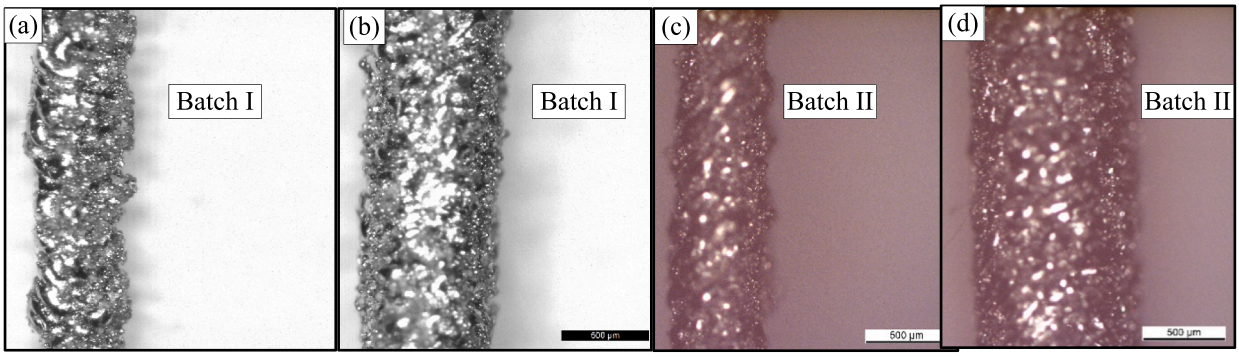

Fig. 5. Examples of the optical microscopy images used to measure the diameter and check the general surface roughness of the rebars for (a) 0.4 mm plain rebar, batch I, (b) 0.8 mm plain rebar, batch I, (c) 0.4 mm plain rebar, batch II, and (d) 0.4 mm plain rebar, batch II.

Table 3
Concrete mixing details.

Mix	Binder	Binder Commercial name	S/B	W/B	Additives
A	Cement	Holcim CEM I 42.5 N (Normo 4)	1.0	0.5	1.0 g of Master Master Glenum ACE30 (Superplasticizer)
B	Gypsum	Prestia Normal Plus Plaster	1.0	1.0	–
C	Gypsum	Prestia Creation Plaster	1.0	1.0	–
D	Gypsum	Prestia Tradition Plaster	1.0	1.0	–
E	Gypsum	Prestia Normal Plus Plaster	1.0	0.7	–
F	Gypsum	Prestia Creation Plaster	1.0	0.5	–
G	Gypsum	Prestia Tradition Plaster	1.0	0.7	–

the cylinder molds, PVC pipes with 15 mm inner diameter were casted with a much larger height and then cut into 30 mm high pieces using a wet cutting table with a cutting saw equipped with a high-quality diamond saw blade. Fig. 6 depicts the cylinder and beam molds. The beam molds were made of two parts to ease demolding after concrete hardening.

Although the cylinder and beam specimens were larger than what would 1:30 scaling of standard specimens require (e.g., typical tested specimens according to ASTM C39 for compression tests and ASTM C78 for four-point bending test), the specimen sizes were close to the dimensions of the components of a 1:30 scaled model of a typical two-story RC building. According to a performed sample design of such building, the columns had cross section of 17 mm x 17 mm while the beams had 17 mm x 20 mm cross section.

3.3. Pullout tests

As noted earlier in this paper, three variations of rebar surface ribs were chosen to cover a range of bond behavior between concrete and reinforcing bars according to Table 2 and Fig. 4. The reason behind testing plain bars is that the 3D printed rebars typically have inherent surface roughness resulting from the manufacturing process and thus were tested to examine the possibility that sufficient bond can be provided by this inherent surface roughness as discussed earlier. The pullout samples were cast in PLA 3D printed molds as is illustrated in Fig. 6. The samples were cubes with side length equal to 25 times the bar nominal diameter. This cube size was chosen to be able to cast concrete into the molds efficiently. The bonded length was 5 times the bar diameter according to the RILEM standard to allow for pullout failure and accordingly allow for investigating the local bond slip behavior. Rebar unbonding was achieved by 3D printing a hollow cylinder along with the bond cube mold (Fig. 6d). A clay paste was used to prevent flow of concrete into the unbonded length of the rebar. No secondary (transverse) reinforcement was used. A plan and elevation views of the pullout samples are shown in Fig. 6 (g and f, respectively). Two rebar diameters were tested; 0.8 mm and 0.67 mm, corresponding to 24 mm and 20 mm at 1:30 scale, respectively. Again, these diameters were chosen as they represent typical longitudinal reinforcement diameters in typical two-story RC frame structure. Similar to beam molds, the pullout sample molds consisted of two parts assembled together to ease demolding. Concrete mix G was chosen for casting the bond samples for reasons that are discussed later in this paper. In addition, mix A was tried since it was the only cement mix. For mix G concrete, all the rib configurations shown in Table 2 were tested while only plain and D1 configurations were tested for with mix A concrete. This was decided since for mix A concrete, the bond behavior of plain and D1 ribbed bars was

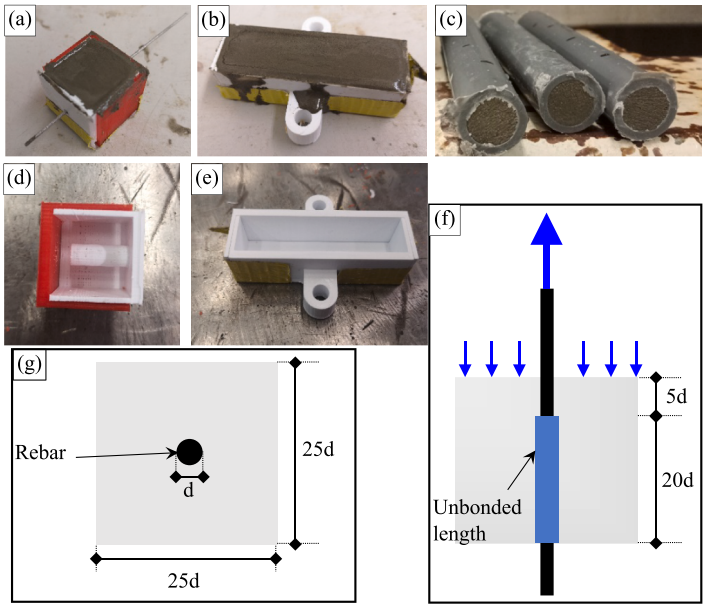

Fig. 6. (a), (b) pullout and four-point bending sample molds while casting (c) PVC pipes used for casting concrete cylinders during cutting (d), (e) empty pullout and four-point bending sample molds (f) schematic drawing (elevation view) for the pullout sample and the loading condition (g) plan view of the pullout sample.

found to be controlled by steel fracture, so there was no merit in testing rebars that would result into even larger bond. Five samples were casted for each configuration, however, during unmolding, some of the samples were either heavily damaged (in the concrete part) or the rebar was heavily bent. These damaged samples were not tested.

4. Test setup and loading protocol

4.1. Tensile test of reinforcing bars

A 200 kN Universal Testing Machine (UTM) at the ETH Zurich was used to perform the tensile tests. Fig. 7a shows the test setup used to perform the tests. A pair of 1 kN tension grips were attached to the machine. The specimens were tested under monotonically increasing displacement with strain rate of 0.015 (1.5 %) (mm/mm)/minute according to [22] until rebar fracture. The strain rate was controlled by the movement of the cross head of the UTM. Strain was measured using an extensometer attached to the rebar. A 10 kN load cell was used to measure the applied load.

4.2. Concrete compression and four-point bending tests

The same 200 kN UTM with the appropriate attachments was used to perform the compression and the four-point bending on concrete samples. The loading was applied with displacement-controlled increments corresponding to a strain rate of 1×10^{-5} mm/mm/second until failure. Such a strain rate was chosen according to [23] so that strain rate does not affect the behavior of the tested samples. For four-point bending test, this strain refers to the outermost fiber of the mid-span cross section of the beam.

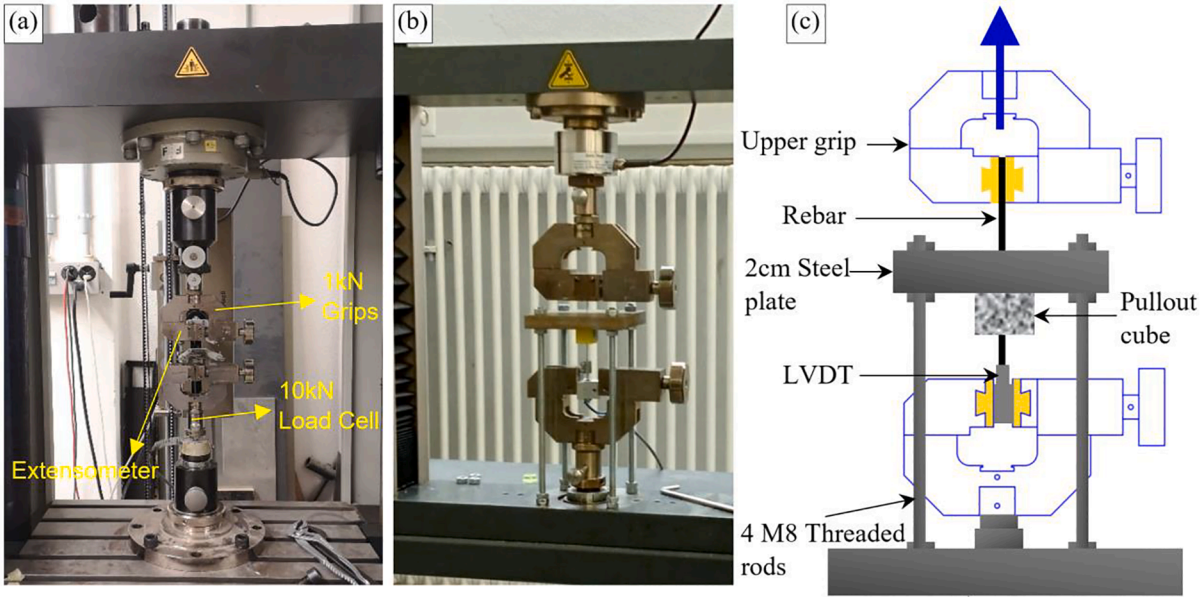

Fig. 7. Test Setup for (a) Tensile tests, (b) and (c) Pull-out Tests.

4.3. Pullout tests

A 10 kN Universal Testing Machine (UTM) at the ETH Zurich was used to perform the pullout tests. Out of the different pull out tests that can be performed [24], tests similar to [25,26] were performed. A steel frame consisting of four M8 threaded rods and a 2 cm steel plate was attached to the testing machine as shown in Fig. 7(b and c). The rebars were pulled using the machine upper grip with testing speed 0.1 mm/minute. The slip was measured using a LVDT that was attached to the rebar using a hollow coupler and the LVDT was fixed using the machine lower grip as illustrated in Fig. 7.

5. Test results

5.1. Tensile test of reinforcing bars

The stress strain relationships of steel rebar batches I, II, and III are shown in Figs. 8, 9, and 10, respectively. The average (AVG) and the variability measured by the coefficient of variation (COV) of the main features of the stress strain relationships is summarized in Table 4. These main features are illustrated in Fig. 11 and they are: 1. Elastic modulus (E_s), 2. Yield strength (f_y), 3. Ultimate strength (f_u), 4. Ratio of ultimate to yield strength (T/Y), 5. Ratio of post yield modulus to elastic modulus (α), and 6. Maximum strain (ε_{su}). Yield strength value was calculated using the offset of 3 ‰ as suggested by the ASTM E8/E8M-21 standard. In addition, the characteristic parameter values according to the Eurocode for design of concrete structures EC2 [27] are shown in Table 4. These values correspond to 5 %, 10 %, and 10 % percentiles for f_y, T/Y, and ε_{su} parameters, respectively. These values are reported to evaluate the degree to which the small-scale 3D printed rebars resemble the full scale rebars and the related design code requirements.

Fig. 12 depicts a summary of the comparison between the characteristic test parameter values with the EC2 recommendations. According to the Eurocode (EC2), reinforcing bars are divided into three classes according to ductility; A, B, and C with A being the least ductile and C being the most ductile. The requirements for ductility of reinforcing bars in EC2 and how conforming are the tested rebars are as follows (see Table 4 and Fig. 12 for reference):

- Characteristic yield strength (f_{yk}) to be in the range of 400 – 500 MPa for all the three ductility classes. The upper limit of the code is imposed for insuring enough ductility since high yield strength can significantly reduce the ductility of RC members. For all the three batches, the deformed (D1) rebars satisfied this requirement. In contrary, the larger diameter (0.8 mm) plain rebars had 390 MPa for batch I and (355 and 350) for batches (II and III), respectively, which is lower than the lower limit of the code range of 400 MPa (87.5 % of the code minimum in the worst case). Moreover, plain rebars had lower strength (yield and ultimate) than deformed rebars for all batches. This might be attributed to the fact that the surface ribs contribute to the overall cross section of the rebars of the specimens, despite the apparent distinction between core and ribs, and thus increase the strength of the bars since the bar core diameter is typically used for strength calculations. For the small diameter (0.4 mm) rebars, the yield strength was smaller than the EC2 minimum (around 85 % of the EC2 minimum, Table 4). Moreover, Mizra & MacGregor [28] and Saputra et al. [29] studied the statistical variation of full-scale reinforcing bar properties. Their results showed a COV of the yield stress ranging from 0.035 to 0.135 depending on grade, diameter, and testing procedure – such COVs are comparable to the ones reported in Table 4. Similar COVs were also shown for 316 stainless steel wires used for model (small scale) reinforcement by Knappett et al. [30].
- The ratio of characteristic ultimate strength to the characteristic yield strength (T/Y ratio) to be at least 1.05, 1.08, 1.15 for ductility classes A, B, and C, respectively. The T/Y ratio is mainly responsible for the distribution of plastic deformation over larger or lower length and avoiding local strain concentrations [31]. Larger T/Y ratios can increase member ductility by increasing the distance over which plastic deformations are distributed [31,32]. All the tested 3D printed bar batches had T/Y ratios of more than 1.10, satisfying the requirements of ductility class B. Moreover, many of the rebars exceeded the 1.15 T/Y ratio required for ductility class C (e.g., all the 0.8 mm diameter deformed bars); an observation that indicates the good ductility properties of the rebars from the T/Y point of view.
- The characteristic ultimate elongation (strain), ε_{suk}, to be at least 2.5 %, 5 %, and 7.5 % for ductility classes A, B, and C, respectively. Along with lower yield strength and high T/Y ratio, increasing the ultimate strain capacity can increase reinforced concrete member ductility. Hassan and Elmorsy [31], based on parametric section analysis based on a typical beam cross section, showed that increasing the ultimate steel strain capacity had the potential of increasing the section ductility by up to 100 %. Increasing the ultimate steel strain capacity from 0.05 to 0.10 yielded about 100 % increase in section curvature ductility [31]. Batch I had high strain capacities ranging from 6.33 % (0.4 mm plain rebar) to 14.06 % (0.8 mm plain rebar) indicating high ductility and satisfying ductility class B (for the 0.4 mm plain rebar) and ductility class C (for other rebars of batch I) requirements. For batches II and III, the deformed bars had higher characteristic strain capacities (3.28 % and 4.12 %

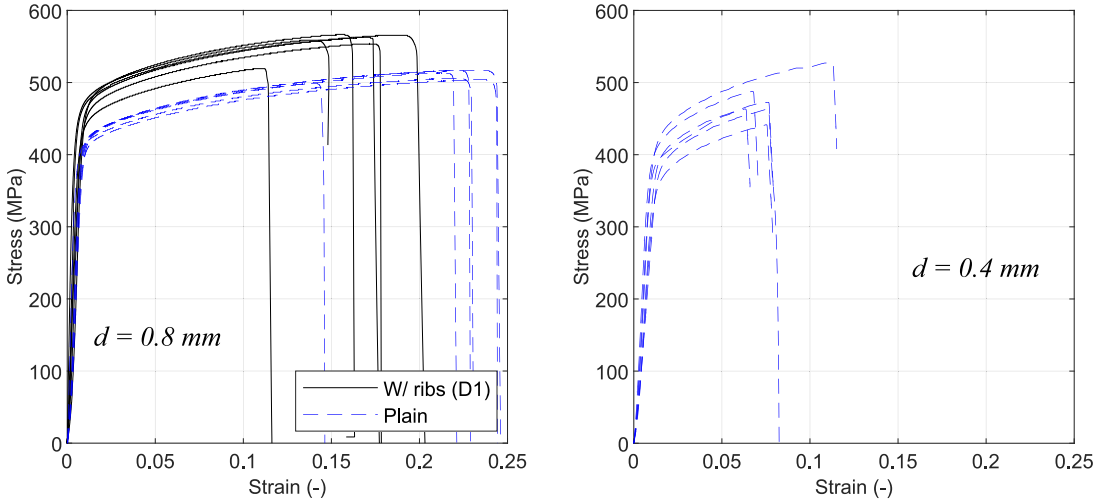

Fig. 8. Stress strain relationships of rebars from Batch I.

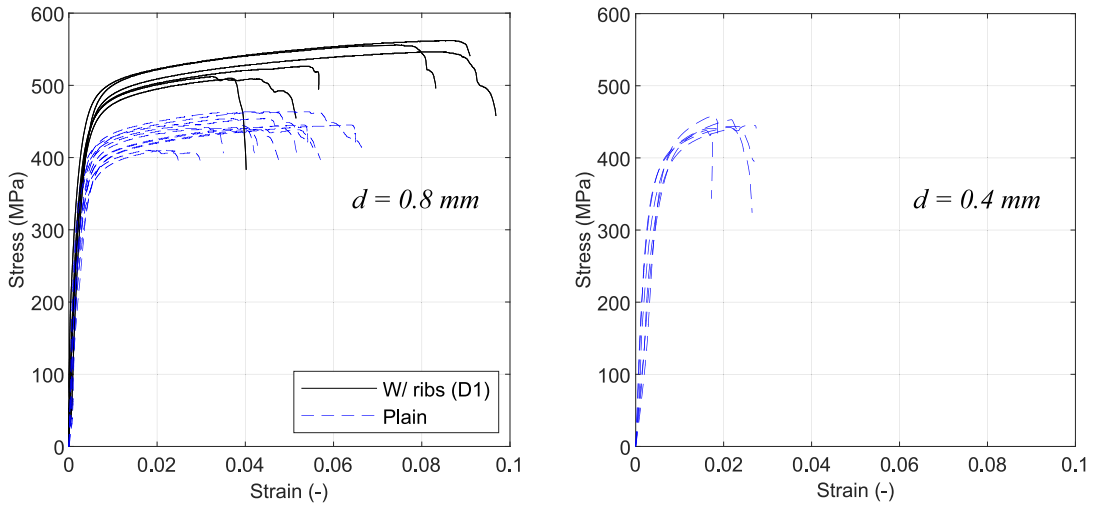

Fig. 9. Stress strain relationships of rebars from Batch II.

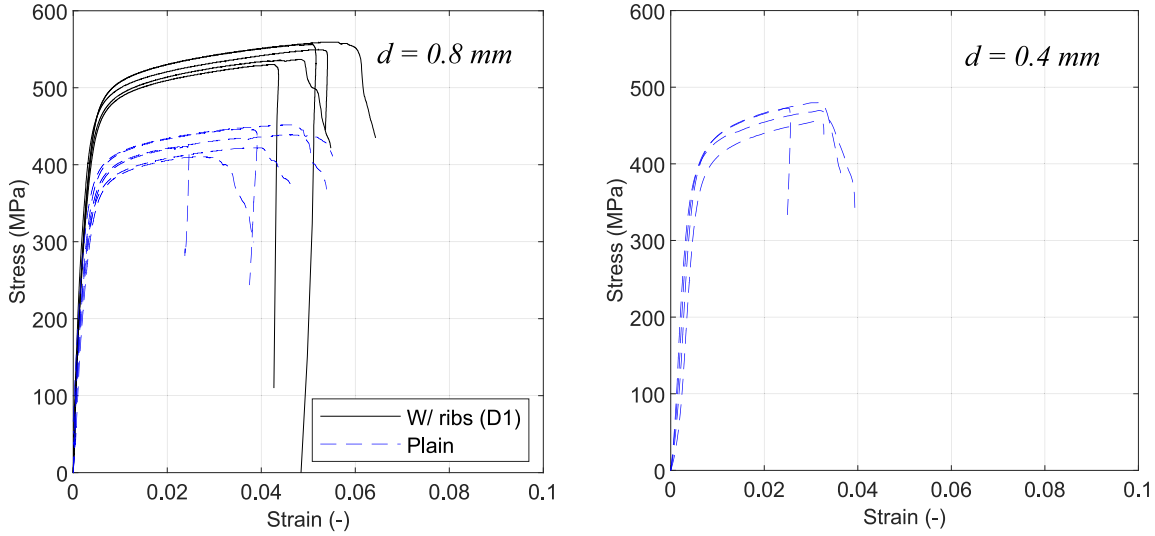

Fig. 10. Stress strain relationships of rebars from Batch III.

for batches II and III, respectively) than plain rebars. The 0.8 mm deformed rebars in batches II and III lied between the requirements of the ductility classes A and B. Taking into consideration that the 0.4 mm plain rebars are intended to model stirrups in the proposed framework, the ductility of these rebars are typically not important, especially for modern structures that are mainly designed to fail in flexural hinging mode. The 0.8 mm plain rebars had low maximum strain capacity – ε_{stuk} was 2.32 and 2.37 for batches II and III, respectively, which is below the limit of the least ductile reinforcing bars class of ductility (class A).

The samples of the first batch showed very low elastic moduli compared to rebars used in RC constructions, which should typically range from 180 to 220 GPa. This is mainly due to the presence of porosity in the bars between the contour and filling as shown in Fig. 3. Therefore, further optimization of the process was conducted, resulting in more reasonable elastic moduli ranging between 175 and 215 MPa for the 0.8 mm samples from batches II and III as discussed earlier. These values compare well with measured Young's moduli values of bulk 316L samples fabricated by LPBF [33,34]. For all batches, the 0.4 mm rebars exhibit lower elastic moduli than their 0.8 mm counterparts. On the one hand, this is might be due to a generally higher amount of porosity in the 0.4 mm bars. Besides, pores of the same size have a more pronounced effect on the mechanical properties if the sample diameter is reduced. On the other hand, this is attributed to a more pronounced texture formation in the thinner bars, resulting in highly anisotropic mechanical properties [33,35]. However, a more detailed study of this phenomenon is beyond the scope of the present study.

On a different note, the variability of the yield strength, ultimate strength, and, accordingly, the T/Y ratio was small (the COV was 6.9 % as a maximum value among the three parameters). On the other hand, the variability of the elastic modulus and maximum strain was generally higher. This high variability in the maximum strain capacity contributed to the low characteristics maximum strain compared to the mean/median values. This high variability may be attributed to the manual removal (with a tweezer) of the support structure that is used during the printing process.

The optimized printing parameters were used to print rebars for pullout testing since they had better quality (less porosity). No heat treatment was applied to the pullout rebars since the pullout specimens were designed to fail in pullout failure which loosely depend on the mechanical properties of the rebars and significantly depend on the surface roughness and deformations of the rebars.

Table 4
Tensile test results summary.

Batch	Nominal Diameter [mm]	Actual Diameter [mm]	Rib configuration	No. of specimens		E_s [MPa]	f_y [MPa]	f_{yk} [MPa]	f_u [MPa]	T/Y [-]	$(T/Y)_k$ [-]	α [%]	ε_{su} [%]	ε_{su} [%]
I	0.80	0.75	P	6	*AVG*	71,375	396.9	390.2	509.3	1.28	1.26	0.71	20.0	14.06
					COV	0.203	0.011	–	0.014	0.014	–	0.193	0.167	–
	0.80	0.75	D1	6	*AVG*	82,848	440.3	411.6	554.5	1.26	1.21	0.68	15.0	10.8
					COV	0.270	0.048	–	0.032	0.048	–	0.281	0.178	–
	0.40	0.33	P	6	*AVG*	40,226	381.9	344.8	476.0	1.25	1.21	2.91	7.8	6.33
					COV	0.183	0.052	–	0.061	0.033	–	0.179	0.212	–
II	0.80	0.96	P	6	*AVG*	198,725	371.7	355.6	442.3	1.19	1.14	0.57	4.2 %	2.32
					COV	0.101	0.053	–	0.041	0.043	–	0.142	0.313	–
	0.80	0.96	D1	6	*AVG*	193,637	452.4	450.9	535.4	1.18	1.12	0.54	6.0	3.28
					COV	0.056	0.032	–	0.042	0.026	–	0.095	0.357	–
	0.40	0.56	P	6	*AVG*	174,340	363.3	339.0	450.9	1.25	1.16	1.88	2.1	1.62
					COV	0.310	0.068	–	0.017	0.069	–	0.459	0.177	–
III	0.80	0.96	P	6	*AVG*	212,712	358.6	349.8	432.4	1.21	1.10	0.69	3.5	2.37
					COV	0.081	0.055	–	0.037	0.028	–	0.223	0.255	–
	0.80	0.96	D1	5*	*AVG*	183,380	465.0	455.5	546.5	1.18	1.16	0.66	4.9	4.12
					COV	0.124	0.020	–	0.023	0.010	–	0.038	0.095	–
	0.40	0.56	P	4*	*AVG*	134,829	385.8	372.6	469.3	1.22	1.19	1.61	3.0	2.52
					COV	0.190	0.035	–	0.022	0.023	–	0.201	0.103	–

*Some rebars were heavily bent and were not tested.

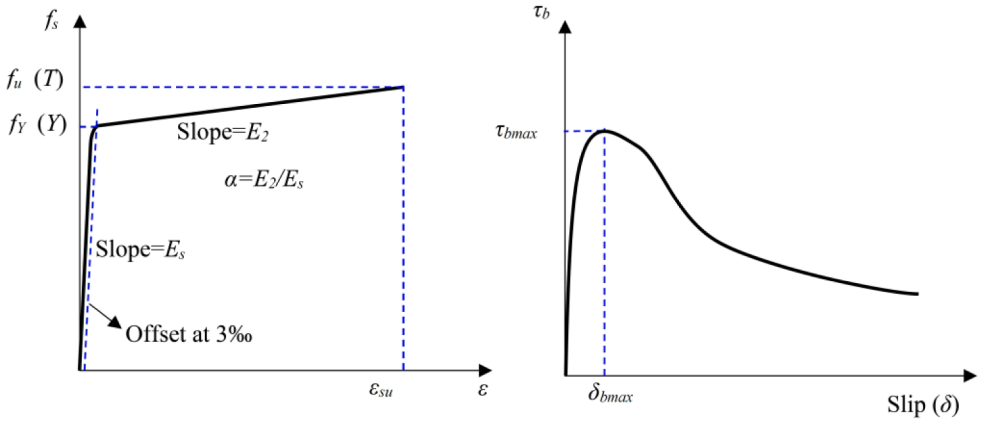

Fig. 11. Illustration of the key parameters of the reinforcing bars stress strain relationship (left) and bond stress slip relationship (right).

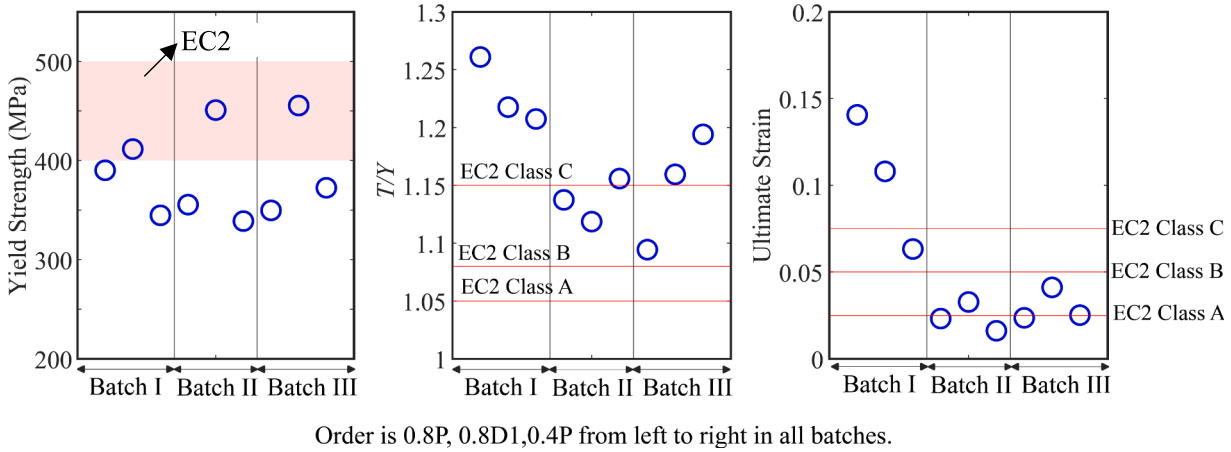

Fig. 12. Comparison between the characteristic test parameter values with the EC2 recommendations for (a) yield strength, (b) T/Y ratio, and (c) ultimate strain capacity.

Table 5
Results of the compression and four-point bending tests.

Mix	Binder	S/B	W/B	f_c (AVG) [MPa]	f_c (COV) [-]	f_r (AVG) [MPa]	f_r (COV) [-]	f_r/f_c (AVG) [-]
A	Cement	1.0	0.5	41.04	0.11	10.38	0.14	0.25
B	Gypsum	1.0	1.0	4.21	0.16	1.42	0	0.34
C	Gypsum	1.0	1.0	−*	−*	2.58	0.06	−*
D	Gypsum	1.0	1.0	5.85	0.10	2.59	0.08	0.44
E	Gypsum	1.0	0.7	6.86	0.21	3.80	0.06	0.55
F	Gypsum	1.0	0.5	22.48	0.04	6.37	0.11	0.28
G^{+}	Gypsum	1.0	0.7	19.93	0.08	4.14	0.04	0.21

*Collapsed during unmolding.
$^{+}$Mix selected for the pullout tests.

5.2. Concrete compression and four-point bending tests

This section discusses the compressive (f_c) and tensile strength (represented by the modulus of rupture, f_r) of the different mixes tried in this paper. Table 5 summarizes the results of the compression and four-point bending tests. The cement concrete was left to cure for 28 days before testing while the gypsum concrete was only left for 14 days. The cement concrete mix had compressive strength 41.04 MPa and the modulus of rupture was 10.38. While such a compressive strength is normal and is frequently encountered in full scale structures, the tensile strength is much higher than the prototype (full scale) strength which is intelligible because of size effects [13]. The measured modulus of rupture is 250 % larger than what ACI 318–19 code [36] predicts ($f_r = 0.62\sqrt{f_c} = 3.97$ MPa). The tensile strength of concrete is an important parameter affecting the concrete strength in diagonal tension and resistance to shear, bond strength with bars, and cracking load levels and crack patterns [13]. Accordingly, proper scaling of tensile strength is vital for replication of failure modes and cracking pattern. This observation motivated the use of other gypsum as a binder instead of cement since it was observed to be less prone to scale effects in previous studies [13,15,16].

For mixes B, C, and D, that had high W/B ratio (W/B = 1.0), the compressive strength was too small and could not be used to physically model realistic prototype concrete. Moreover, the ratio of modulus of rupture to compressive strength (average values) was very high (0.34–0.44). For gypsum-based mixes E, F, and G, that had lower W/B ratios, as recommended by the plaster manufacturer, the average compressive strength was much higher reaching 22.48 MPa for mix F and 19.93 MPa for mix G. Mix E still had lower than needed average compressive strength (6.86 MPa). Focusing on Mixes F and G as they reasonable compressive strengths, mix G was selected for the pullout test since it had reasonable compressive and tensile strength and, accordingly, was expected to have reasonable bond behavior with the 3D printed rebars. For mix G, the COV for the compressive strength and modulus of rupture were 0.08 and 0.04, respectively. Comparing to prototype scale, the modulus of rupture of mix G was 4.14 MPa, which makes it only 49 % larger than what ACI 318–19 code [36] predicts ($f_r = 0.62\sqrt{f_c} = 2.77$ MPa) – indicating an improvement compared to mix A.

5.3. Pull-out tests

The optimized printing parameters (from batch II and III) were used to print the rebars used in the pullout test. In addition, two concrete mixes were used; mix A and mix G. All the pullout samples made with mix A (cement plaster) failed in rebar fracturing mode. Plain rebars and rebars with ribs D1were tested first. According to the failure mode observed in them, it was decided not test bars with D2 and D3 ribs since they would also fail in bar fracture mode, as their surface is rougher. The bar fracture mode prohibits acquiring bond stress slip relationships since the bond strength between the rebar and the concrete is not triggered. Accordingly, the results of pullout test results with mix A are not further discussed in this paper. The main conclusion in this regard is that the cement plaster mix had too high bond. This too high bond, along with high tensile strength of the mix A concrete, can significantly affect the cracking pattern of concrete since it results in concentrated plastic deformations in the rebar at few crack locations which leads to premature fracture of rebars limiting the ductility of RC members. This phenomena of concentrated cracking and premature failure of reinforcing bars have been observed in a recent study by Del Giudice et al. [14] in which the behavior of RC 1:40 scale columns with additively manufactured rebars were tested under cyclic loading simulating earthquake excitations. The main results of mix A concrete pullout results are summarized in Table 6.

For mix G, Figs. 13 and 14 depict the bond stress slip relationships for the 0.8 mm and 0.67 rebars, respectively. The bond stress is calculated as (l_b is the bar bonded length and F is the applied force):

$$\tau = \frac{F}{\pi d l_b}$$

In order to evaluate the degree of similarity between the local bond stress slip relationship of the tested model scale materials and their prototype scale counterparts, various models from literature are utilized. Again, only the results of mix G concrete pullout tests are discussed. Moreover, the comparison will focus to pullout failure mode, since other failure modes (splitting and bar yielding/fracture) were not observed. These models are as follows:

1. Fib model code 2010 (fib MC10) [37] bond slip model (for plain and deformed rebars)

Fig. 15 depicts a typical idealization for the bond slip relationship for deformed and plain rebars as suggested by *fib* MC10. It should be noted that the idealized model represents the average bond-slip behavior of the *fib* TG4.5 and ACI 408 bond test database as discussed in detail in [17]. Therefore, it is not a sort of conservative design model, but can be used as an average approximation of realistic prototype bond-slip behavior. For deformed rebars, the idealization is typically a four-segment curve while for plain rebars, it is a two-segment curve. The definition of the four segments of the bond stress slip for deformed and plain rebars is as follows:

$$\tau_b = \tau_{b\max}(s/s_1)^{\alpha} \text{ for } 0 \leqslant s \leqslant s_1 \quad (1)$$

$$\tau_b = \tau_{b\max} \text{ for } s_1 \leqslant s \leqslant s_2 \quad (2)$$

$$\tau_b = \tau_{b\max} - (\tau_{b\max} - \tau_{bf})\,(s - s_2)/(s_3 - s_2) \text{ for } s_2 \leqslant s \leqslant s_3 \quad (3)$$

$$\tau_b = \tau_{bf} \text{ for } s_3 < s \quad (4)$$

where $\tau_{bf} = 0.4\tau_{b\max}$, $\tau_{b\max} = 2.5\sqrt{f_{cm}}$ for good bond conditions, and $\tau_{b\max} = 1.25\sqrt{f_{cm}}$ for all other bond conditions in the case of ribbed rebars and. For the plain surface rebars, $\tau_{b\max} = 0.3\sqrt{f_{cm}}$ for good bond conditions and $\tau_{b\max} = 0.15\sqrt{f_{cm}}$ for all other bond conditions. For the deformed rebars, the corner slips (S_1, S_2, and S_3 – see Fig. 15) are 1 mm, 2 mm, and c_{clear} (the clear distance between ribs) for good bond conditions and 1.8 mm, 3.6 mm, and c_{clear} for all other bond conditions. For the plain surface rebars, $S_1 = S_2 = S_3 = 0.1$ mm for good and all other bond conditions and $\tau_{b\max} = \tau_{bf}$. This translates to a single ascending branch until $\tau_{b\max}$ and then constant strength of $\tau_{b\max}$ for strains after S_3

Table 6
Summary of the pullout test results.

Concrete Mix	Diameter [mm]	Rib Configuration	Number of specimens	τ_{bmax} (AVG) [MPa]	τ_{bmax} (COV) [-]	$\tau_{bmax}/\sqrt{f_c}$ (AVG) [MPa$^{0.5}$]	δ_{bmax} (AVG) [mm]	Failure mode
A	0.80	P	4	29.8	0.023	4.65	0.218	Rebar fracture*
	0.80	D1	4	24.3	0.185	3.79	0.171	Rebar fracture
	0.67	P	–**	–**	–**	–**	–**	Rebar fracture
	0.67	D1	4	32.7	0.0214	5.10	0.136	Rebar fracture
G	0.80	P	4	5.1	0.155	1.15	0.5745	Pullout
	0.80	D1	3	10.2	0.0437	2.29	0.1350	Pullout
	0.80	D2	5	8.05	0.119	1.80	0.1975	Pullout
	0.80	D3	5	9.6	0.058	2.16	0.7411	Pullout
	0.67	P	1	7.9	–***	1.77	0.2354	Pullout
	0.67	D1	4	6.5	0.111	1.47	0.3048	Pullout
	0.67	D2	3	7.3	0.246	1.63	0.0678	Pullout
	0.67	D3	4	7.3	0.128	1.64	0.4880	Pullout

* Since the rebar fractured, the reported strength and slip values corresponds to the maximum shear stress developed.
** These specimens had a problem in casting; some concrete flowed into the unbonded length (were checked after testing).
***Only one datapoint.

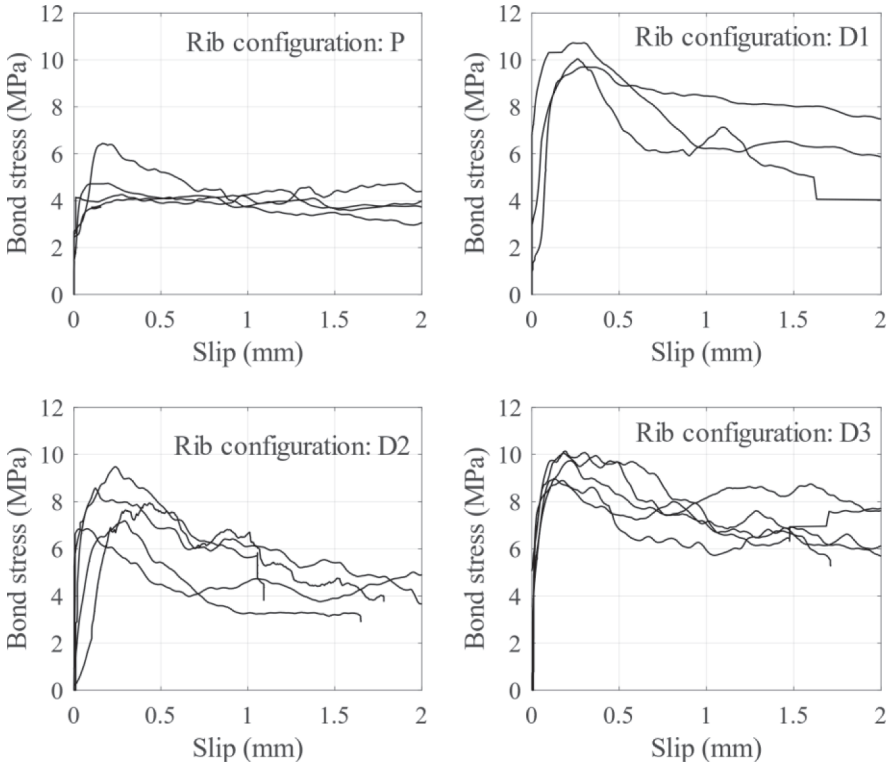

Fig. 13. Bond stress-slip relationships for bars with diameter 0.80 mm.

in the case of plain rebars. The factor α is 0.4 for deformed rebars and 0.5 for plain rebars. The background to the *fib* bond stress slip models is explained in [17].

2. Harajli et al. (1995) [38] model (for deformed rebars only):

Harajli et al. suggested a similar model to the *fib* MC10 for deformed rebars with a few modifications. These modifications are as follows: 1. $\tau_{bmax} = 2.57\sqrt{f_{cm}}$ 2. $\tau_{bf} = 0.35\tau_{bmax}$ 3. $S_1 = 0.15\ c_{clear}$, $S_2 = 0.3\ c_{clear}$ $S_3 = c_{clear}$ 4. $\alpha = 0.3$. The model does not contain any reduction for other than good bond conditions.

3. Cairns 2021 [39]: for plain rebars (for plain rebars only):

Cairns developed a bond stress slip model that addressed some of the drawbacks of the *fib* MC10 model for plain rebars. The main drawbacks addressed are that the *fib* model did not contain any reduction in bond capacity after the peak point, unlike the test data. Moreover, the bond strength values in *fib* MC10 seemed highly conservative based on the database used by [39]. Cairns suggested a model consisting of two branches; one ascending and one descending branch. The model is shown in Fig. 15. The two branches had the same equation as Equation (1) with $\alpha = 0.2$ and -0.2 for the ascending and descending branches, respectively. Moreover, Cairns suggested a shear strength of $\tau_{bmax} = 1.08\sqrt{f_{cm}}$.

It is worth mentioning here that these models were developed for much larger bar diameters than the ones tested in this study and mostly, they are not applicable to the cases tested. However, the approach used to check the similarity between the bond behavior of the model scale rebars and their prototype scale counterparts is based on assuming a scale factor (here, 1:30) and accordingly scaling up the tested specimens to the prototype scale (e.g., the rebars 0.8 mm and 0.67 mm to 24 mm

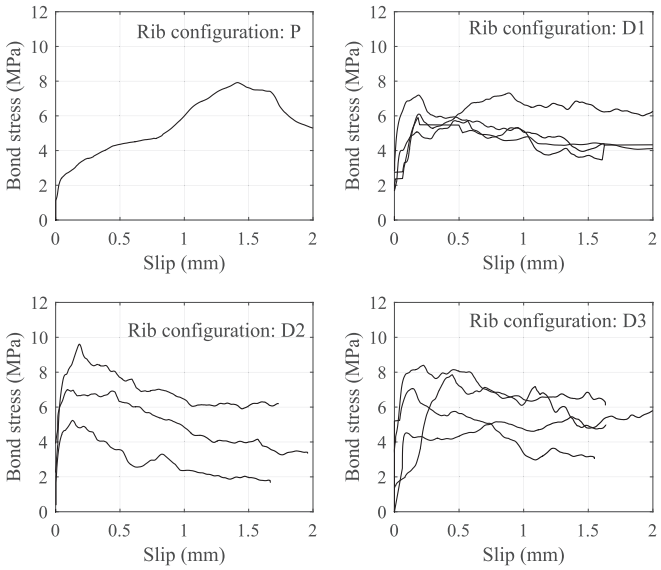

Fig. 14. Bond stress-slip relationships for bars with diameter 0.67 mm.

and 20 mm). Afterwards, the full-scale dimensions are used to establish target bond stress slip relations and the test results are compared to this target relations.

Figs. 16 and 17 depict a comparison between the bond stress-slip relationships from the test and from the literature idealized models for bars with diameter 0.8 mm and 0.67 mm, respectively. Fig. 18 shows a comparison between tested bond strength and the bond strength suggested by the different literature models. The uncertainty of the *fib* MC10 in this figure is based on the test database of the *fib code* committee [17]. For the *fib* MC10 model for plain rebars, only the good bond conditions case is shown since this model is already too conservative even for the good bond conditions case as shown by [39].

The bond stress in these figures (Figs. 16 through 18) is normalized by $\sqrt{f_c}$; a typical normalization in most of the empirical relationships (from literature) discussed in this paper. Through Figs. 16 to 18, the following observations can be made:

- For the plain rebars, the inherent roughness seemed not sufficient to provide bond strength comparable to full scale ribbed surface rebars especially for the 0.8 mm rebar. For the 0.67 mm plain rebar, only one specimen was tested and more data are needed to confirm this observation. However, the inherent roughness resulted in a bond which is higher that the bond between prototype plain rebars and concrete.
- Relatively small differences were observed among the three rib configurations (D1, D2, and D3). The difference between the maximum and minimum test average bond strength (among the three rib configurations) was around 27 % and 11 % for the 0.80 and the 0.67 mm rebars, respectively.
- For all three deformed rebars (D1:D3), the drop of bond stress after reaching its peak was smaller than what the *fib* model dictates for prototype concrete. For the time being, this is a drawback of the physical model, that could potentially be improved in the future by trying different model concrete mixes and different rib sizes. However, it is quantifiable and it can be considered in numerical modelling by adjusting the parameters of the *fib* model.
- For ribbed rebars, the 0.67 mm rebar had lower average bond strength than the 0.8 mm rebars for all the three rib configurations. This is in contrast to the size effect of bonding strength in prototype RC, where smaller rebars exhibit larger bond strength. It can be explained by the accuracy of the printer. Attempting to print details, such as ribs, on such the small diameter rebar (0.67 mm rebar), reaches the limits of the accuracy of the printer. The ribs of the 0.67 mm rebar were proportionally smaller.
- Bars with ribs D1 and D3 had the best match (on average) with full scale normalized bond strength for the 0.8 mm bar (2.29 $MPa^{0.5}$ and 2.16 $MPa^{0.5}$) while for the 0.67 mm rebar, D2 and D3 had the best match (1.63 $MPa^{0.5}$ and 1.64 $MPa^{0.5}$), respectively. According to the *fib* model, the relevant normalized value is 2.5 $MPa^{0.5}$.
- For all ribbed rebars, the ultimate bond strength lied between the good and other bond conditions required by the *fib* MC10.
- Similar conclusions are observed for the Harajli 1995 model as in the *fib* MC10.
- For plain rebars, the normalized shear strength was 1.15 $MPa^{0.5}$ and 1.77 $MPa^{0.5}$ for diameters 0.8 mm and 0.67 mm, respectively, which correspond 1.06 and 1.64 times the more realistic Cairns 2021 model for plain rebars.

It is noteworthy that the standard deviation of the *fib* MC10 model for deformed rebars in Fig. 18 is based on [17].

6. Conclusions

This paper explored the potential of using metal 3D printing to manufacture the reinforcement of small-scale (on the order of 1:30) physical models of Reinforced Concrete structures, which can be used for centrifuge testing within the framework of Earthquake Engineering. It performed tension tests of sub-millimeter diameter rebars, compression and 4-point bending tests of model concrete, as well as pull out tests of reinforcing bars with and without ribs. The main conclusions are:

a) The tensile behavior or the reinforcing bars of 0.4 mm and 0.8 mm can be physically similar to the behavior of prototype reinforcement

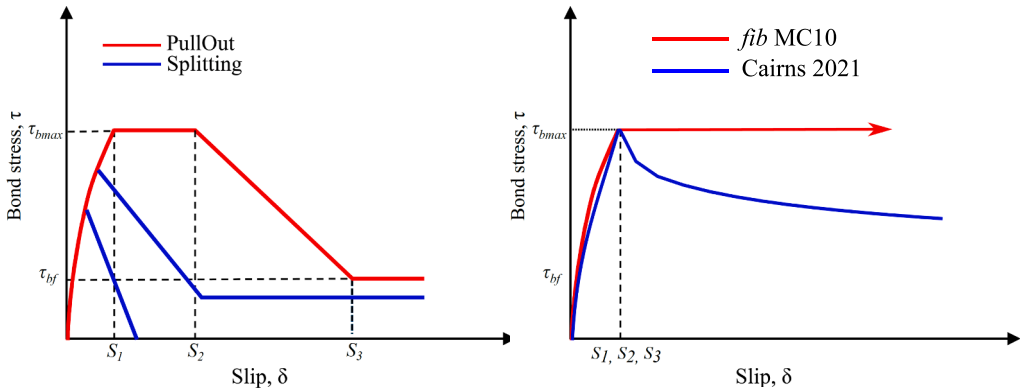

Fig. 15. Typical idealization of the bond stress slip relationship for deformed rebars (left) and plain rebars (right).

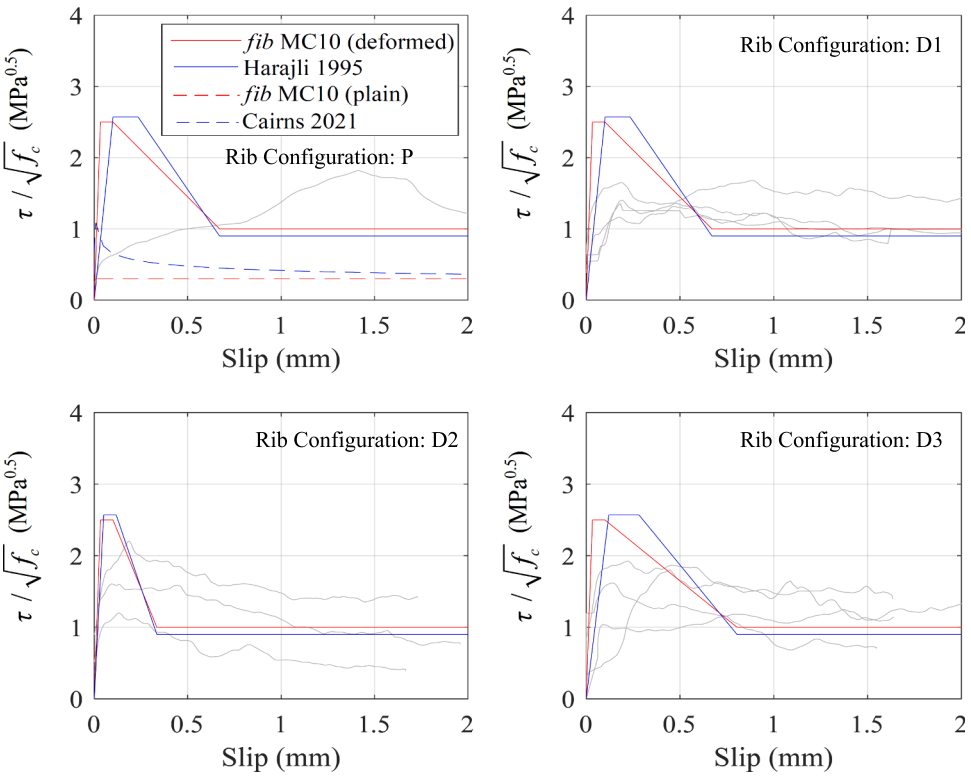

Fig. 16. Comparison between the bond stress slip relationships from the test and from other literature idealized models the for bars with diameter 0.80 mm.

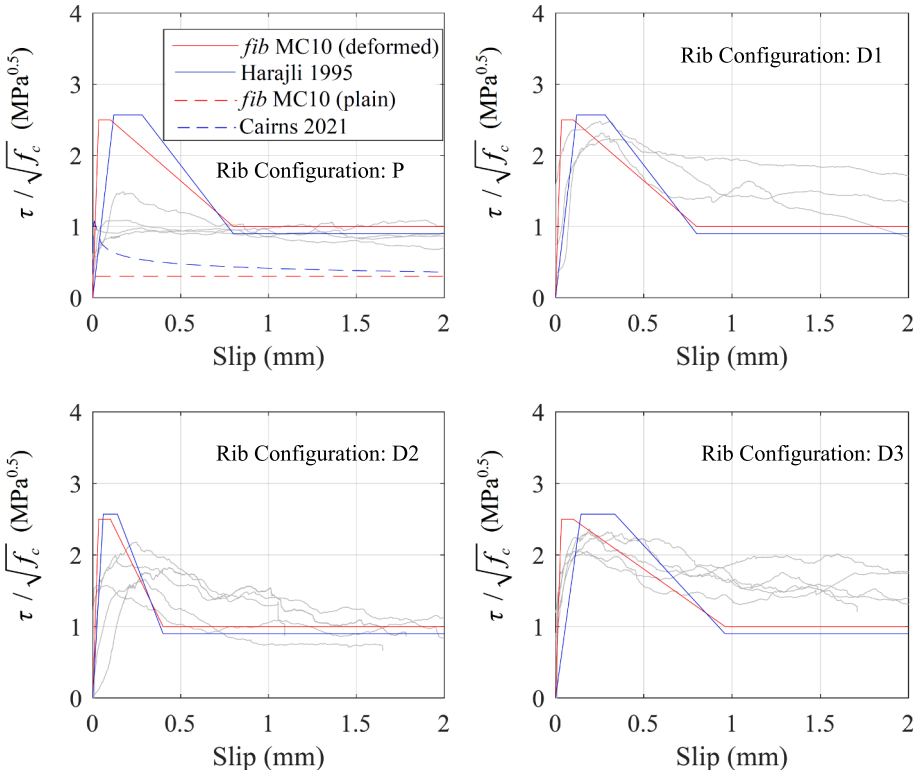

Fig. 17. Comparison between the bond stress slip relationships from the test and from other literature idealized models the for bars with diameter 0.67 mm.

in terms of their tensile yield strength, ultimate strength, ultimate elongation, and pre- and post-yield elastic modulus. This holds both for characteristic values and for the dispersion. However, this encouraging behavior strongly depends on the printing parameters, that needs to be fine-tuned to avoid printing porous reinforcement that will unavoidably be of reduced strength and stiffness, hence of lower similarity to the prototype ones. It should also be noted that the presented results are valid for bars that are printed at 45° to the

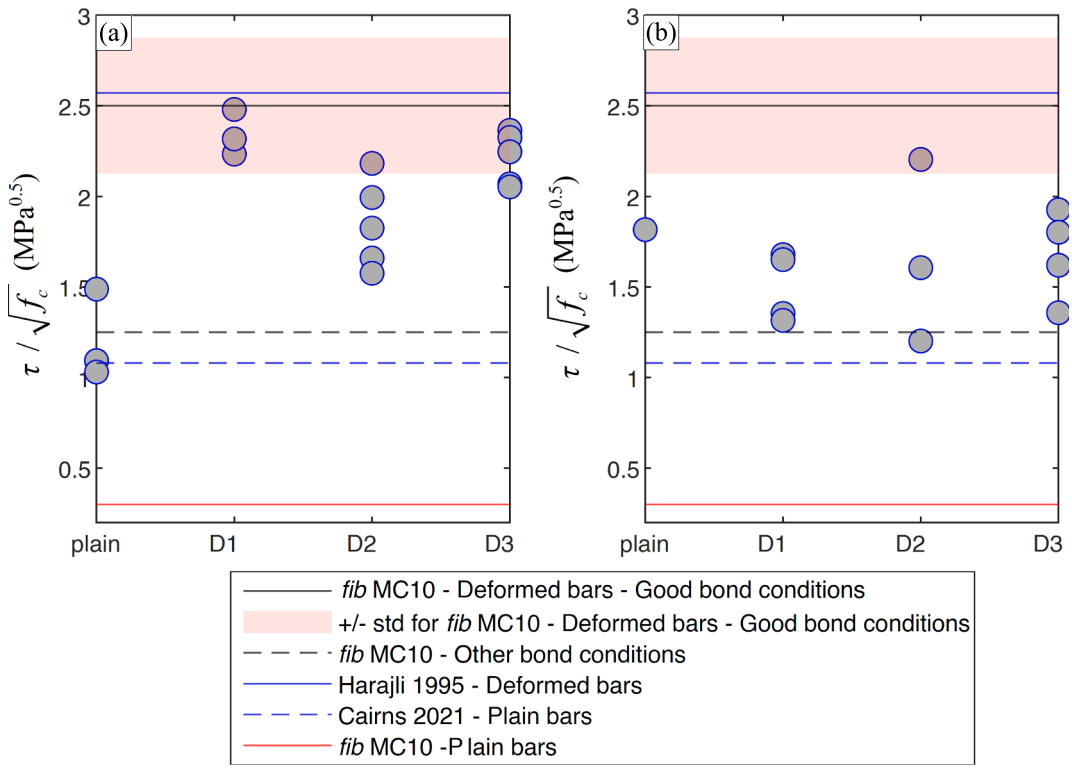

Fig. 18. Comparison between tested bond strength and the bond strength suggested by different literature models for (a) 0.8 mm rebars and (b) 0.67 mm rebars.

base plate – other orientations are likely to have different mechanical properties which requires further study. However, in the planned system-level, all reinforcement is planned to printed with the same orientation as the tested bars (45°).

b) The gypsum mix seems to be of higher similarity to prototype concrete in terms of compressive and tensile strength, supporting the use of such mixes in previous research (e.g., [15;16]). The tensile strength is not to be overlooked, because if it is too high, then the bond between the rebars and the concrete will be unrealistically high, resulting in strain localization (compared to prototype concrete) and premature fracture of the rebars [40].

c) Pull-out tests showed that despite rebars inherent roughness, printing ribs is a necessity to physically model the bonding behavior between prototype ribbed rebars and concrete – at least for model mixes of the observed tensile strength. Between the different rib configurations that were tested there was none that behaved remarkably better. They all managed to achieve a bond strength similar to the bond strength of prototype RC, despite being less able to physically model the drop of the bond strength with increasing slip. This is a notable improvement compared to previous studies [14], where the bond strength of the model was too high, something that led to strain localization and premature rupture of the rebars, when testing model beams.

CRediT authorship contribution statement

Medhat Elmorsy: Writing – original draft, Visualization, Validation, Methodology, Investigation, Formal analysis, Data curation. **Rafal Wrobel:** Writing – review & editing, Validation, Methodology, Investigation. **Christian Leinenbach:** Writing – review & editing, Validation. **Michalis F. Vassiliou:** Writing – review & editing, Supervision, Resources, Project administration, Methodology, Funding acquisition, Conceptualization.

Declaration of competing interest

The authors declare that they have no known competing financial interests or personal relationships that could have appeared to influence the work reported in this paper.

Data availability

Data will be made available on request.

Acknowledgements

This work was supported by the ETH Zurich under grant ETH-11 21-1. The advice of Mariana Loli (Senior Consultant at Grid Engineers, Athens, Greece) on casting the gypsum concrete is greatly appreciated.

References

[1] P. Moncarz, H. Krawinkler, Theory and Application of Experimental Model Analysis in Earthquake Engineering, Department of Civil Engineering, Stanford University, California, John A. Blume Earthquake Engineering Center, 1981.
[2] T. Paret, A. Shuck, Performance-Based Design Procedures: Beware Uncharted Waters, 16th European Conference on Earthquake Engineering, Thessaloniki, 2018.
[3] M. Panagiotou, J.I. Restrepo, Displacement-Based Method of Analysis for Regular Reinforced-Concrete Wall Buildings: Application to a Full-Scale 7-Story Building Slice Tested at UC-San Diego, J. Struct. Eng. 137 (2011) 677–690, https://doi.org/10.1061/(ASCE)ST.1943-541X.0000333.
[4] M. Trüb, Numerical modeling of high performance fiber reinforced cementitious composites, IBK Bericht, ETH Zurich, 2011.
[5] X. Lin, X. Lu, Numerical models to predict the collapse behavior of RC columns and frames, The Open Civ. Eng. J. 11 (2017) 854–860, https://doi.org/10.2174/1874149501711010854.
[6] B.A. Bradley, A critical examination of seismic response uncertainty analysis in earthquake engineering, Earthq. Eng. Struct. Dyn. 42 (2013) 1717–1729, https://doi.org/10.1002/eqe.2331.
[7] W. Kim, A. El-Attar, R.N. White, Small-scale modeling techniques for reinforced concrete structures subjected to seismic loads, National Center for Earthquake Engineering Research Washington, DC, 1988.
[8] J. Bachmann, M. Strand, M.F. Vassiliou, M. Broccardo, B. Stojadinovic, Is rocking motion predictable? Earthq. Eng. Struct. Dyn. 47 (2018) 535–552, https://doi.org/10.1002/eqe.2978.

[9] M.F. Vassiliou, M. Broccardo, C. Cengiz, M. Dietz, L. Dihoru, S. Gunay, K. M. Mosalam, G. Mylonakis, A. Sextos, B. Stojadinovic, Shake table testing of a rocking podium: Results of a blind prediction contest, Earthq. Eng. Struct. Dyn. 50 (2021) 1043–1062, https://doi.org/10.1002/eqe.3386.
[10] C. Zhong, C. Christopoulos, Scaled shaking table testing of higher-mode effects on the seismic response of tall and slender structures, Earthq. Eng. Struct. Dyn. 52 (2023) 549–570, https://doi.org/10.1002/eqe.3772.
[11] A.A. Katsamakas, M.F. Vassiliou, Finite element modeling of free-standing cylindrical columns under seismic excitation, Earthq. Eng. Struct. Dyn. 51 (2022) 2016–2035, https://doi.org/10.1002/eqe.3651.
[12] Z.P. Bazant, J. Planas, Fracture and size effect in concrete and other quasibrittle materials, 1st Edition, CRC Press, New York, 1997. https://doi.org/10.1201/9780203756799.
[13] H.G. Harris, G. Sabnis, Structural modeling and experimental techniques, CRC Press, Boca Raton, 1999.
[14] L. Del Giudice, R. Wróbel, A.A. Katsamakas, C. Leinenbach, M.F. Vassiliou, Physical modelling of reinforced concrete at a 1: 40 scale using additively manufactured reinforcement cages, Earthq. Eng. Struct. Dyn. 51 (2022) 537–551, https://doi.org/10.1002/eqe.3578.
[15] M. Loli, J.A. Knappett, M.J. Brown, I. Anastasopoulos, G. Gazetas, Centrifuge modeling of rocking-isolated inelastic RC bridge piers, Earthq. Eng. Struct. Dyn. 43 (2014) 2341–2359, https://doi.org/10.1002/eqe.2451.
[16] J. Knappett, C. Reid, S. Kinmond, K. O'Reilly, Small-scale modeling of reinforced concrete structural elements for use in a geotechnical centrifuge, J. Struct. Eng. 137 (2011) 1263–1271.
[17] J. Cairns, Bond and anchorage of embedded steel reinforcement in fib Model Code, Struct. Concr. 16 (2015) (2010) 45–55.
[18] W.E. Frazier, Metal additive manufacturing: a review, J. Mater. Eng. Perform. 23 (2014) 1917–1928.
[19] T. DebRoy, H.L. Wei, J.S. Zuback, T. Mukherjee, J.W. Elmer, J.O. Milewski, A. M. Beese, A.D. Wilson-Heid, A. De, W. Zhang, Additive manufacturing of metallic components–process, structure and properties, Prog. Mater. Science. 92 (2018) 112–224, https://doi.org/10.1016/j.pmatsci.2017.10.001.
[20] Y.M. Wang, T. Voisin, J.T. McKeown, J. Ye, N.P. Calta, Z. Li, Z. Zeng, Y. Zhang, W. Chen, T.T. Roehling, R.T. Ott, Additively manufactured hierarchical stainless steels with high strength and ductility, Nat. Mater. 17 (2018) 63–71, https://doi.org/10.1038/nmat5021.
[21] EN:10080, Steel for reinforcement of concrete – weldable reinforcing steel. 2005.
[22] Astm e8, e8m-22,, Standard test methods for tension testing of metallic materials, ASTM International (2022).
[23] J.B. Mander, M.J. Priestley, R. Park, Theoretical stress-strain model for confined concrete, J. Struct. Eng. 114 (1988) 1804–1826, https://doi.org/10.1061/(ASCE)0733-9445(1988)114:8(1804).
[24] Aci prc-408-03,, Bond and Development of Straight Reinforcing Bars in Tension, American Concrete Institute (2003 (Reapproved 2012).).
[25] J. Murcia-Delso, A. Stavridis, P.B. Shing, Bond Strength and Cyclic Bond Deterioration of Large-Diameter Bars, ACI Struct. J. 110 (2013).
[26] M. Deng, J. Pan, H. Sun, Bond behavior of steel bar embedded in Engineered Cementitious Composites under pullout load, Constr. Build. Mater. 168 (2018) 705–714.
[27] European Committee for Standardisation (CEN), Eurocode 2: Design of Concrete Structures. Part 1: General Rules and Rules for Buildings, 2004.
[28] S.A. Mirza, J.G. MacGregor, Variability of mechanical properties of reinforcing bars, ASCE J. of the Structural Division 105 (1979) 921–937.
[29] A. Saputra, E. Limsuwan, T. Ueda, Characteristics of material and fabrication for concrete structures in Indonesia, Engineering Journal 14 (2010) 11–22.
[30] J.A. Knappett, , L. Shields, , A.H. Al-Defae, , M. Loli, & Brown, M.J. 2018. Variability of small scale model reinforced concrete and implications for geotechnical centrifuge testing. Proc. 9th Int. Conf. on Physical Modelling in Geotechnics 2018, London, UK, 17-20 July 2018, CRC Press, 1: 241-246. ISBN 978-1-138-34419-8.
[31] W. Hassan, M. Elmorsy, Database trends and critical review of seismic performance tests on high strength steel reinforced concrete components, Eng. Struct. 239 (2021) 112092.
[32] D. Sokoli, Fracture of high-strength bars in concrete frame members under earthquake loads, The University of Texas at Austin, 2018. Doctoral Dissertation,.
[33] L. Hitzler, J. Hirsch, B. Heine, M. Merkel, W. Hall, A. Öchsner, On the Anisotropic Mechanical Properties of Selective Laser-Melted Stainless Steel, Materials. 10 (2017) 1136, https://doi.org/10.3390/ma10101136.
[34] E. Garlea, H. Choo, C.C. Sluss, M.R. Koehler, R.L. Bridges, X. Xiao, Y. Ren, B. H. Jared, Variation of elastic mechanical properties with texture, porosity, and defect characteristics in laser powder bed fusion 316L stainless steel, Mater. Sci. Eng. A 763 (2019) 138032.
[35] A. Leicht, C. Pauzon, M. Rashidi, U. Klement, L. Nyborg, E. Hryha, Effect of part thickness on the microstructure and tensile properties of 316L parts produced by laser powder bed fusion, Advances in Industrial and Manufacturing Engineering. 2 (2021) 100037, https://doi.org/10.1016/j.aime.2021.100037.
[36] ACI (American Concrete Institute). Building code requirements for structural concrete, ACI 318-19 and Commentary ACI 318R-19. Farmington Hills, MI, 2019.
[37] Fédération Internationale du Béton (fib). fib Model Code for Concrete Structures 2010, Lausanne, Switzerland, 2012.
[38] M. Harajli, M. Hout, W. Jalkh, Local bond stress-slip behavior of reinforcing bars embedded in plain and fiber concrete, ACI Mater. J. 92 (1995) 343–353.
[39] J. Cairns, Local bond–slip model for plain surface reinforcement, Struct. Concr. 22 (2021) 666–675.
[40] P. Marti, M. Alvarez, W. Kaufmann, V. Sigrist, Tension chord model for structural concrete, Struct. Eng. International 8 (1998) 287–298, https://doi.org/10.2749/101686698780488875.